

A new mechanochemical model for apical constriction: coupling calcium signalling and viscoelasticity

Katerina Kaouri^{1,*}, Neophytos Christodoulou², Abhishek Chakraborty¹, Paul E. Méndez³, Paris Skourides² and Ricardo Ruiz-Baier^{4,5,6}

¹ School of Mathematics, Cardiff University, Cardiff, United Kingdom

³ School of Biological Sciences, University of Cyprus

² Research Centre on Mathematical Modelling (MODEMAT), Escuela Politécnica Nacional, Quito, Ecuador

⁴ School of Mathematics & Victorian Heart Institute, Monash University, Melbourne, Australia

⁵ World-Class Research Center “Digital biodesign and personalized healthcare”, Sechenov First Moscow State Medical University, Moscow, Russia

⁶ Research Core on Natural and Exact Sciences, Universidad Adventista de Chile, Chillán, Chile

Correspondence*:

School of Mathematics, Cardiff University, Cardiff CF24 4AG, United Kingdom

kaourik@cardiff.ac.uk

2 ABSTRACT

Embryonic epithelial cells exhibit strong coupling of mechanical responses to chemical signals and most notably to calcium. Recent experiments have shown that the disruption of calcium signals during neurulation strongly correlates with the appearance of neural tube defects. We, thus, develop a multi-dimensional mechanochemical model and use it to reproduce important experimental findings that describe anterior neural plate morphogenetic behaviour during neural tube closure. The governing equations consist of an advection-diffusion-reaction system for calcium concentration which is coupled to a force balance equation for the tissue. The tissue is modelled as a linear viscoelastic material that includes a calcium-dependent contraction stress. We implement a random distribution of calcium sparks that is compatible with experimental findings. A finite element method is employed to generate numerical solutions of the model for an appropriately chosen range of parameter values. We analyse the behaviour of the model as three parameters vary: the level of IP_3 concentration, the strength of the stretch-sensitive activation and the maximum magnitude of the calcium-dependent contraction stress. Importantly, the simulations reproduce important experimental features, such as the spatio-temporal correlation between calcium transients and tissue deformation, the monotonic reduction of the apical surface area and the constant constriction rate, as time progresses. The model could also be employed to gain insights into other biological processes where the coupling of calcium signalling and mechanics is important, such as carcinogenesis and wound healing.

21 **Keywords:** calcium signalling, viscoelasticity, computational modelling, mechanobiology, embryology, numerical methods.

1 INTRODUCTION

During the early stages of the development of an embryo's central nervous system (CNS), neuroepithelial cells undergo a shape change via apical constriction (AC), a morphogenetic process controlled by apical actomyosin contraction that is induced by calcium transients [1, 2]. AC results in the folding of the neural plate and in the formation of the neural tube. It is not fully understood how AC in the neural plate is controlled and how it contributes to tissue morphogenesis but recent experiments have shown that Ca^{2+} plays a crucial role in regulating AC during neural tube closure (NTC) [1, 2]. Furthermore, pharmacologically inhibiting Ca^{2+} has been shown to lead to neural tube defects [1, 3, 4], such as *Spina Bifida* and anencephaly.

Many experiments have documented that intracellular Ca^{2+} release triggers actomyosin-based contractions, in both embryonic and cultured cells [1, 5, 6, 2, 4]. The ability of cells to sense and respond to forces by elevating their cytosolic Ca^{2+} is also well established; mechanically stimulated Ca^{2+} waves have been observed propagating through ciliated tracheal epithelial cells [7, 8, 9], rat brain glial cells [10, 11, 12], developing epithelial cells in *Drosophila* wing discs [13] and many other cell types [14, 15, 16, 17]. Thus, different types of mechanical stimuli, from shear stress to direct mechanical stimulation, can elicit Ca^{2+} elevation (although the sensing mechanism may differ in each case). Moreover, localisation of stresses or strains within the cells can generate alteration in patterns of Ca^{2+} distribution in a tissue by changing cell displacement magnitude, direction, and velocity [18, 19]. This is especially noteworthy since distinct Ca^{2+} signalling patterns differentially modulate AC for efficient epithelial folding. The latter mechanism has a broad range of physiological outcomes [2].

Since mechanical stimulation elicits Ca^{2+} release and Ca^{2+} elicits contractions which are sensed as mechanical stimuli by the cell, a two-way mechanochemical feedback between Ca^{2+} and contractions should be at play. Motivated by the recent experimental observations [1, 2] where, during AC, increasing tension in the contracting cells yields Ca^{2+} release which, in turn, elicits contractions in the cells which are sensed as mechanical stimuli by the neighbouring cells, we develop a new mechanochemical model that captures the interplay of Ca^{2+} signalling and mechanical forces during AC.

This paper extends the mechanochemical model in [20], which describes the coupling of Ca^{2+} signalling with the mechanics of the embryonic epithelial tissue during AC in one spatial dimension; it also extends the multi-dimensional model presented in [21]. In the aforementioned models, following the early mechanochemical models in [22], where small strains are assumed, the embryonic tissue is assumed to be a linear viscoelastic (Kelvin–Voigt) solid (with one elastic spring and two viscous dashpots), where only after the initial stress has vanished, does the material go back to its original state. Also, In the model proposed here, as in [20, 21, 22, 23], we assume that the viscoelastic stress includes an active contraction stress which depends on the cytosolic Ca^{2+} concentration. The models in [20, 21], as well as the model presented here, employ the well-established Ca^{2+} signalling model from Atri *et al.* [24], called the "Atri model" hereafter. The Atri model captures the experimentally verified Ca^{2+} -induced Ca^{2+} release (CICR) process. It consists of two differential equations, one PDE for the cytosolic Ca^{2+} concentration and another PDE for the percentage of the non-inactivated IP_3 receptors on the endoplasmic reticulum (ER) which allow release of Ca^{2+} from the ER into the cytosol.

In Figure 1.1 we show still images from a time lapse recording of the anterior neural plate during the last stage of neural tube closure (stage 16 of *Xenopus* embryo development). For live imaging, 4-cell stage *Xenopus laevis* embryos were injected with the mRNA encoding membrane-GFP and the calcium sensor GECO-RED at the two dorsal blastomeres to target the neural tissue. Subsequently the embryos were

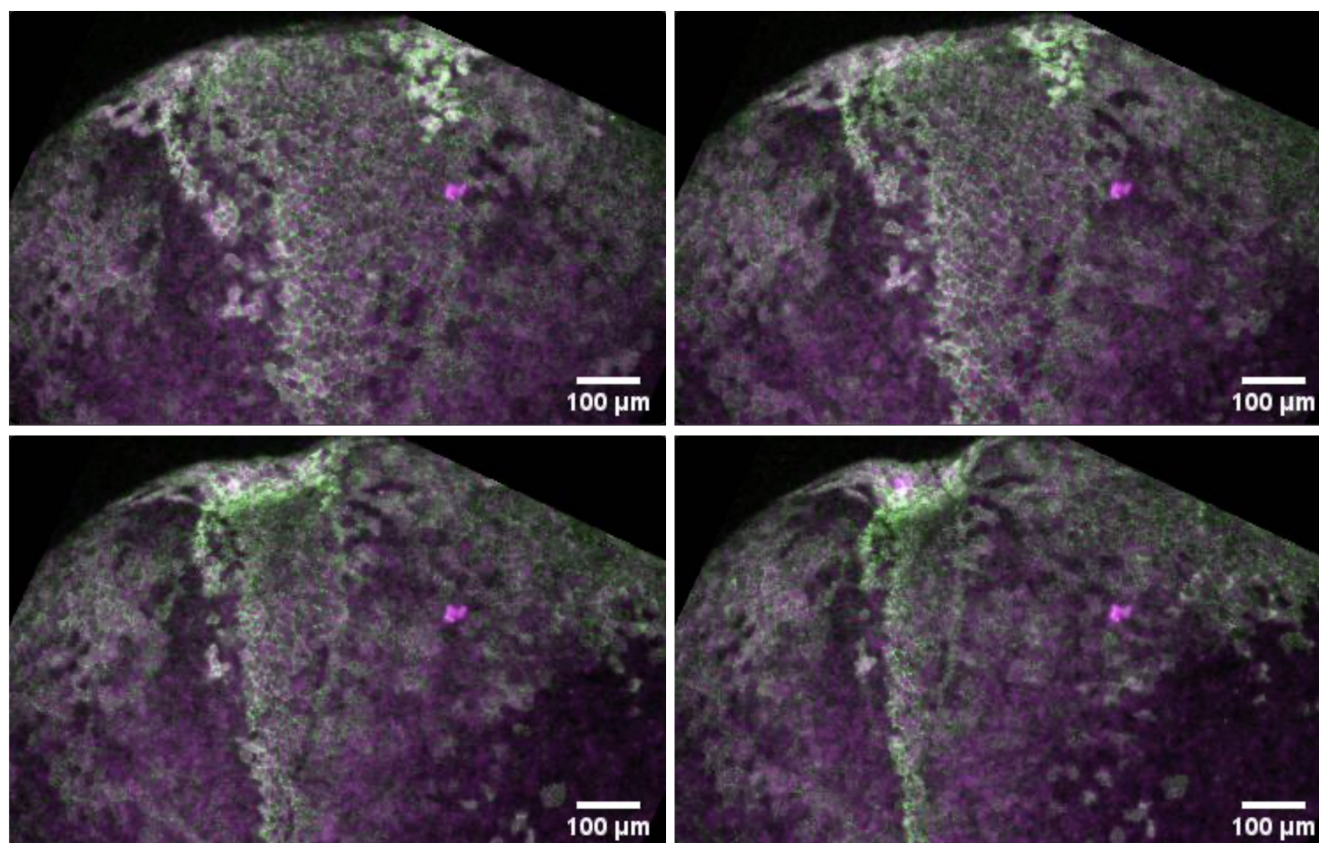


Figure 1.1. Snapshots of the closure of the neural tube over a period of 55 minutes (from top-left to bottom-right). The green colour indicates the cell membrane and magenta is the calcium sensor.

64 allowed to develop until stage 14 and imaged during neural tube closure. The time lapse recordings of
 65 neural tube closure that we represent in Fig 1.1 were generated on a ZEISS LSM 710 confocal microscope
 66 with a 30 seconds time interval. At this stage, the ectoderm of the embryo consists of the neuroepithelium,
 67 which is surrounded by the surface ectoderm. The last stage of anterior neural tube closure is controlled
 68 by AC of neuroepithelial cells [1] and lasts about 40 minutes; this is the stage we model here. During
 69 AC cells reduce their apical surface area and change their shape from columnar to a wedge shape [1].
 70 These cell shape changes subsequently drive the bending of the neuroepithelium and the formation of the
 71 neural tube. Note that the frequency of calcium transients has been quantified in [1]. The observation there
 72 is that the frequency increases as neural tube closure progresses. This information ties up with the data
 73 presented also in [20]. Thus, experimental evidence shows a clear correlation between the appearance of
 74 calcium transients, and the reduction of the apical surface area during neural tube closure. Even though the
 75 process of AC is three-dimensional we focus attention to the stage where the apical surface area reduces
 76 (in a ratchet-like manner). This is the active driver of the process and it is sufficient to describe it with a
 77 two-dimensional model, as we do below. For stage 16 of *Xenopus* embryo development studied here we
 78 can assume small strains; hence the tissue can be modelled as a linear Kelvin–Voigt viscoelastic solid. This
 79 linear viscoelastic material is completely defined by the stiffness and viscosity, which can be determined
 80 using diverse measuring approaches such as pipette suction, optical laser tweezers, microrheology tools,
 81 particle tracking, or even contact-free techniques [25]. In the present mechanochemical model, we assume
 82 that the viscoelastic stress includes a contraction stress which depends on Ca^{2+} concentration, following
 83 the formulation in [20, 21, 22, 23].

The new mechanochemical model proposed here, following [21] is underpinned also by the following fundamental assumptions: a) the equilibrium of the mechanics in the system is established by a quasi-static balance of linear momentum using displacements and hydrostatic or solid pressure (the so-called Herrmann formulation [26]). The introduction of solid pressure contributes to achieve robustness in the nearly incompressible regime assumed for the tissue. This occurs when the Poisson ratio approaches 0.5, implying that the first Lamé parameter defining the dilation properties of the material is very large. Also, the mechanochemical coupling is modelled directly in the viscoelastic stress through a Hill function that depends on Ca^{2+} and through the modification of the reaction kinetics by volume change. The two-way coupling mechanism we adopt follows the model structure used in [20, 21, 27, 28, 29, 30].

Finding closed-form solutions to this inherently highly nonlinear and multidimensional problem is only possible in very restricted scenarios and simplified settings. We, hence, resort to solving the governing equations numerically, via an implicit, fully coupled finite element method [21, 30]. Following [21], we nondimensionalise the model using experimentally verified parameter values from neuroepithelial cells undergoing AC during NTC [24, 31, 32] to investigate whether our model reproduces important features of NTC observed in the experiments of [1].

This paper is organised as follows. In Section 2 we present a new mechanochemical model capturing the coupling of calcium signalling to forces in a deforming embryonic epithelial tissue undergoing AC. We also present the computational implementation of the model, using a Finite Element Method. Next, in Section 3 we present the simulations and discuss how they reproduce important experimental features. Finally, Section 4 includes our conclusions and future research directions.

2 METHODS

2.1 A new mechanochemical model coupling calcium signalling and mechanics for apical constriction

Here, we present a new mechanochemical model coupling calcium and mechanics in AC. We adapt, as previously, the Atri *et al.* model [24] to write the governing equations for the cytosolic calcium concentration and the percentage of non-inactivated IPR—for more details on this well-established model see [24, 20, 21]. We also assume, as previously, that the tissue is represented by a linear viscoelastic, Kelvin–Voigt material [20, 21, 22]. The system is assumed to be in mechanical equilibrium, that is the contraction forces generated by the calcium are in mechanical equilibrium with the viscoelastic forces. The model is as follows:

$$\partial_t c + \partial_t \mathbf{u} \cdot \nabla c - D \nabla^2 c = f(c, h, \mathbf{u}) \quad \text{in } \Omega \times (0, t_{\text{final}}], \quad (2.1a)$$

$$\partial_t h + \partial_t \mathbf{u} \cdot \nabla h = g(c, h) \quad \text{in } \Omega \times (0, t_{\text{final}}], \quad (2.1b)$$

$$-\text{div}(\boldsymbol{\epsilon}(\mathbf{u}) - p\mathbf{I} + \alpha_1 \partial_t \boldsymbol{\epsilon}(\mathbf{u}) - \alpha_2 \partial_t p \mathbf{I} + T(c)\mathbf{I}) = \mathbf{0} \quad \text{in } \Omega \times (0, t_{\text{final}}], \quad (2.1c)$$

$$p + \frac{\nu}{(1 - 2\nu)} \text{div } \mathbf{u} = 0 \quad \text{in } \Omega \times (0, t_{\text{final}}], \quad (2.1d)$$

where $[\text{Ca}^{2+}] = c$ is the cytosolic calcium concentration, h is the percentage of non-inactivated IPR, \mathbf{u} is the tissue displacement and p is the Herrmann pressure. ν is the Poisson's ratio and α_1 and α_2 are the shear and bulk viscosities, respectively, and D is the diffusion coefficient of cytosolic calcium. The Cauchy stress has elastic, viscous, and active calcium-dependent stress components. The active stress and the reaction

kinetics are specified as follows:

$$T(c) = \beta_1 \frac{c^n}{\beta_2 + c^n}, \quad f(c, h, \mathbf{u}) = I_{\text{rand}}(\mathbf{x}, t) \mu h K_1 \frac{b+c}{1+c} - \frac{Gc}{K+c} + \lambda \operatorname{div} \mathbf{u}, \quad g(c, h) = \frac{1}{1+c^2} - h.$$

The function I_{rand} multiplying the CICR Ca^{2+} flux is a random-in-space distribution of Ca^{2+} sparks which increases in frequency and in amplitude with time, observed in the experiments of [1]. Since there is a (thin) circumferential layer of epidermal cells surrounding the neuroepithelial cells, the Young's modulus, E , is discontinuous across the interface of these two regions [33]. Hence, we assume that the Young's modulus in the domain is given by

$$E = E_{\text{in}} \chi_{\Omega_{\text{in}}} + E_{\text{out}} \chi_{\Omega_{\text{out}}},$$

where χ_M denotes the characteristic function on the generic subdomain M , and by E_{in} and E_{out} we denote the Young modulus in the inner and outer regions, respectively.

The model parameters and their values are discussed in more detail in Section 2.2.

The PDE system (2.1) is complemented with appropriate initial data for c , h , u and p , respectively given by

$$c(0) = c_0, \quad h(0) = h_0 = \frac{1}{1+c_0^2}, \quad \mathbf{u}(0) = \mathbf{0}, \quad p(0) = 0, \quad \text{in } \Omega, \quad (2.2)$$

where c_0 is the steady state value of c . We also assume stress-free and zero-flux boundary conditions on the domain boundary, as follows:

$$(\epsilon(\mathbf{u}) - p\mathbf{I} + \alpha_1 \partial_t \epsilon(\mathbf{u}) - \alpha_2 \partial_t p \mathbf{I} + T(c)\mathbf{I})\mathbf{n} = \mathbf{0} \quad \text{and} \quad D\nabla c \cdot \mathbf{n} = 0 \quad \text{on} \quad \partial\Omega \times (0, t_{\text{final}}]. \quad (2.3)$$

These pure-traction boundary conditions necessitate imposing an additional condition to render the system well-defined. We, hence, impose that the displacements are orthogonal with respect to the space of rigid motions, that is

$$\mathbb{RM}(\Omega) := \{\mathbf{v} \in \mathbf{H}^1(\Omega) : \epsilon(\mathbf{v}) = \mathbf{0}\}. \quad (2.4)$$

Note that $T(c)$ in (2.1c) has an opposite sign to that in the models of [20, 21]. There, the opposite sign corresponded to dilation instead of contraction here (see also [22, 34]).

2.2 Model parameter values

The Atri Ca^{2+} signalling model we use [24] captures the Ca^{2+} release to the cytosol via the IPR/ Ca^{2+} channels, relying on experimental data from the *Xenopus laevis* oocyte. We nondimensionalised this model in detail in [20]; here we present it in its nondimensional form, choosing the same parameter values.

The values of the mechanical parameters were taken from *Xenopus* and *Drosophila* embryos [31, 32, 35, 33] and are collected in Table 2.1. (The parameter values can be taken from two different species since the magnitude of sub-cellular forces are similar across species.) To determine the Young's modulus and viscosity of neural tissues, in [35] the authors measured the stiffness of dorsal isolate explants of *Xenopus laevis* embryos over different stages of development, from gastrulation to neurulation. They recorded the values of Young's modulus and viscosity over five dorsal isolate explants taken from stage 16 embryos. We averaged these five values to obtain E_{in} . To determine the Young's modulus for the

Parameter list			
Parameter	Definition	Value	Source
E_{in}	Young's modulus on the neural plate	44.26 Pa	[35]
$E_{\text{out}} = 0.55E_{\text{in}}$	Young's modulus on the epidermal layer	24.34 Pa	[33, 35]
T_0	Traction stress	50 – 450 Pa	[36, 37, 38]
ν	Poisson's ratio	0.4	[31, 39]
$\tilde{\alpha}_1$	Shear viscosity	3790 Pa s	[31, 35]
$\tilde{\alpha}_2$	Bulk viscosity	550 Pa s	[31, 35]

Table 2.1. Parameter values for the mechanochemical model.

epidermal cells surrounding the neuroepithelium, E_{out} , we use the ratio between the stiffness moduli of the neuroepithelium and epidermis, as determined in [33]; we, thus, estimate $E_{\text{out}} = 0.55E_{\text{in}}$.

We determine the shear and bulk viscosities, $\tilde{\alpha}_1$ and $\tilde{\alpha}_2$ using data from [35] and [31]. In [35], measurements were taken from five neurulating embryos and we determined the value of net viscosity to be the average of the five values. This net viscosity value was then split using the ratio between the shear and bulk viscosity given in [31].

For the Poisson's ratio, we assume, as in [35], that the embryonic tissue is a *nearly* incompressible material and hence we set $\nu = 0.4$. This value is also consistent with the range of values in [31] and in other experimental studies, e.g. [39]. The value of the maximum (saturation) traction stress, T_0 , is difficult to determine but experiments on zebrafish primordium tissue suggest that the value can range from 50 Pa to 450 Pa [36]. This range is supported by [37] and [38] where traction force microscopy revealed the average traction stresses of cells on 2D substrates to be between 100 Pa and 1000 Pa. In our model, T_0 was set by tuning its value while keeping all other parameter values constant.

The area of a single neuroepithelial cell at the start of apical constriction is $\approx 250\mu\text{m}^2$. We have 256 cells [2] tightly packed in the tissue and, hence, the initial tissue area is approximately $64000\mu\text{m}^2$. We assume that the tissue is a disc-shaped domain of radius $\approx 143\mu\text{m}$. The spatial variables have been non-dimensionalised using $L = 100\mu\text{m}$. Thus, the tissue is represented as a disc of radius $R = 1.43$ in non-dimensional terms.

We take the non-dimensional parameters from [20], as follows: $D = 0.004$, $K_1 = 46.28$, $G = 5.71$ and $K = 0.14$. The three parameters we are going to vary in the simulations are:

$$\mu, \lambda, \text{ and } \beta_1 = \frac{T_0(1+\nu)}{E}. \quad (2.5)$$

As the Young modulus, E , is discontinuous across the interface of the neuroepithelium and the epidermis, so are the parameters α_1 , α_2 and β_1 . From the nondimensionalisation it arises that $\alpha_1 = \frac{(1+\nu)}{E\tau_j} \tilde{\alpha}_1$ and $\alpha_2 = \frac{(1+\nu)(1-2\nu)}{E\nu\tau_j} \tilde{\alpha}_2$, where $\tau_j = 2\text{s}$ and other values as in Table 2.1. On the neuroepithelium we, hence, have $\alpha_1^{\text{in}} = 59.94$ and $\alpha_2^{\text{in}} = 4.35$, whereas on the epidermis we take $\alpha_1^{\text{out}} = 113.67$, $\alpha_2^{\text{out}} = 8.25$.

2.3 Computational implementation of the model using the finite element method

The mechanochemical model (2.1c)-(2.1b) has been discretised using the finite element method (FEM). The open-source FEM library FEniCS [40] was used to obtain the numerical approximation of the variational formulation of the governing equations. Due to the nonlinear nature of the model, the Newton–Raphson method was used and at each iteration the linear tangent system was solved with the MUMPS direct solver [41]. Time derivatives were approximated by a fully implicit backward differencing scheme. A mixed finite element formulation based on the MINI element [42] was used for the numerical approximation of the displacement and the rescaled Herrmann pressure, and piecewise linear and overall continuous elements for the calcium concentration and IPR. The rigid motions in a finite-dimensional subspace of (2.4) were removed from the set of admissible displacements using a Lagrange multiplier approach, as described in [21]. For the Newton–Raphson iterative algorithm, a tolerance of 10^{-8} was used. Note that, as long as an appropriate discrete inf-sup condition is satisfied and one can still construct a suitable auxiliary discrete problem to remove rigid motion solutions, high-order elements can also be used, for example generalised Taylor–Hood elements of degree $k \geq 2$ for the approximation of displacement and rescaled Herrmann pressure, and piecewise polynomials of order k for the approximation of calcium and IPR concentrations. For the lowest-order Taylor–Hood elements one has an additional order of convergence with respect to the MINI-element. That is, we expect an improvement in model predictions as the mesh is refined, but at the price of solving a larger system at each Newton–Raphson iteration. More details about the code can be found in [21, 30].

3 RESULTS AND DISCUSSION

In this section we present numerical solutions of the model for a range of parameter values and explore the agreement of the model with experimental results. We treat μ , λ and β_1 as bifurcation parameters and identify the set of values for which the model exhibits agreement with the experimental results in [1]. The computational domain is a disk of radius $R = 1.43$, discretised into an unstructured triangular mesh of 34947 elements. A fixed time-step of $\Delta t = 0.1$ is used in all simulations.

In order to generate the random field of calcium sparks, I_{rand} , we impose a frequency linearly increasing from 0.1 to 0.4 and set the amplitude to $1 + a_{\text{mpl}}$, with a_{mpl} increasing from 0.47 to 0.78 quadratically—see Figure 3.1. A single spark at the domain centre is included in all simulations.

We proceed to extract transients of the model variables c , h , p , \mathbf{u} at 80 points which are located in a square of side 0.25, centred at the origin. We then average these values over space to generate the evolution of the system over time. The simulations are presented in Figures 3.2–3.3. Figure 3.2 shows the results obtained when $\beta_1^{\text{in}} = T_0(1 + \nu)/E_{\text{in}} = 3.16$, that is when $T_0 = 100$ Pa. When $\mu = 0.288$ the Atri model [24, 20] does not exhibit oscillatory behaviour. The increase of the Herrmann pressure (and of the displacement) is monotonic, which indicates a monotonic contraction and area reduction, as observed in experiments [1, 2]. Hence, our model reproduces this key experimental feature. This behaviour occurs because the random-in-space calcium sparks (modelled by I_{rand}) exist elsewhere in the domain and increase in amplitude and frequency as time progresses (see Figure 3.1).

Increasing T_0 to 250 Pa gives $\beta_1^{\text{in}} = 7.91$. In this case we see in Figure 3.3 that the pressure and displacement approximately double in magnitude compared to those for $T_0 = 100$ Pa ($\beta_1^{\text{in}} = 3.16$).

In all Figures 3.2–3.3, as time advances the Herrmann pressure increases and the tissue contracts and the area decreases monotonically. However, for any fixed value of μ , the contraction decreases as λ

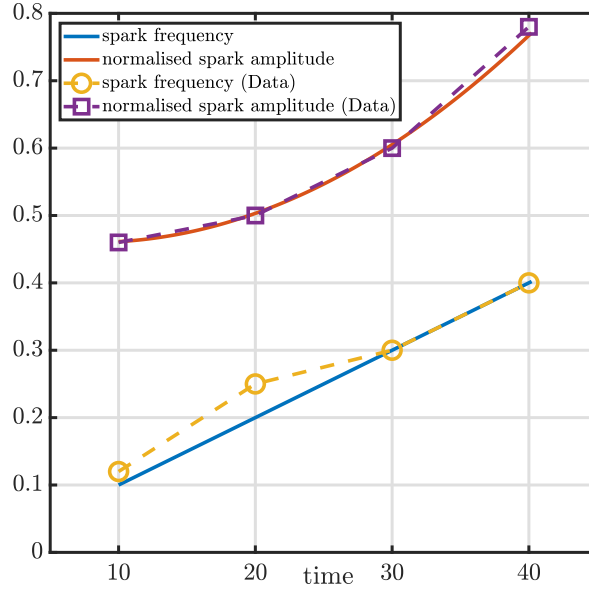


Figure 3.1. Frequency and normalised amplitude of calcium sparks versus time used to construct I_{rand} , fitted to experimental data from [20].

increases. Since λ is a measure of the strength of the coupling between the calcium signalling system and the mechanics of the tissue this result indicates that the stronger the coupling the smaller the contraction.

In Figure 3.4 we plot the tissue area as time progresses. We compute the area using the expression $\int_{\Omega} \det(\mathbf{I} + \nabla \mathbf{u}) d\mathbf{x}$, and compare it with the experimental data in Figure 3.1. In the top left plot, for $\beta_1^{\text{in}} = 7.91$ we plot the area decrease as μ and λ vary. We get a good fit with the area in Figure 3.1 for $\mu = 0.288$ and $\lambda = 0.5$ (yellow line), as seen in Figure 3.3.

For the chosen parameters $\mu = 0.288, \lambda = 0.5$, in the top right plot, we determine the area for $\beta_1^{\text{in}} \in \{1.58, 3.16, 4.74, 7.91\}$ (corresponding to $T_0 = 50, 100, 150, 250$ Pa and changing accordingly β_1^{out}); we see that the area reduction is quite sensitive to the choice of the active contractile force parameter, T_0 , which confirms the nonlinear nature of the model. In the bottom plot the red dash-dotted curve depicts the constriction rate (rate of area reduction) for the parameters $\mu = 0.288, \lambda = 0.5, \beta_1^{\text{in}} = 7.91$. The constriction rate is approximately constant, as identified in the experiments of [1].

In Figure 3.5 we visualise the deformation of the tissue (disc domain) and the associated calcium distribution, at different times. The boundary of the initially non-deformed disc is also shown, for comparison. For $\lambda = 0.01$ we observe nucleation of calcium waves - synchronous waves that are sustained for a longer time. In Figure 3.5 we clearly visualise what has been already noted in Figure 3.3: that, as time advances the area always decreases monotonically and that the larger λ is the smaller the contraction.

In Figure 3.6, for the same set of parameters, $\mu = 0.288, \beta_1^{\text{in}} = 7.91$, and varying λ , we plot all field variables at the time $t = 35$ (to show a different time snapshot than the ones depicted before). For all cases, a larger displacement is observed near the boundary.

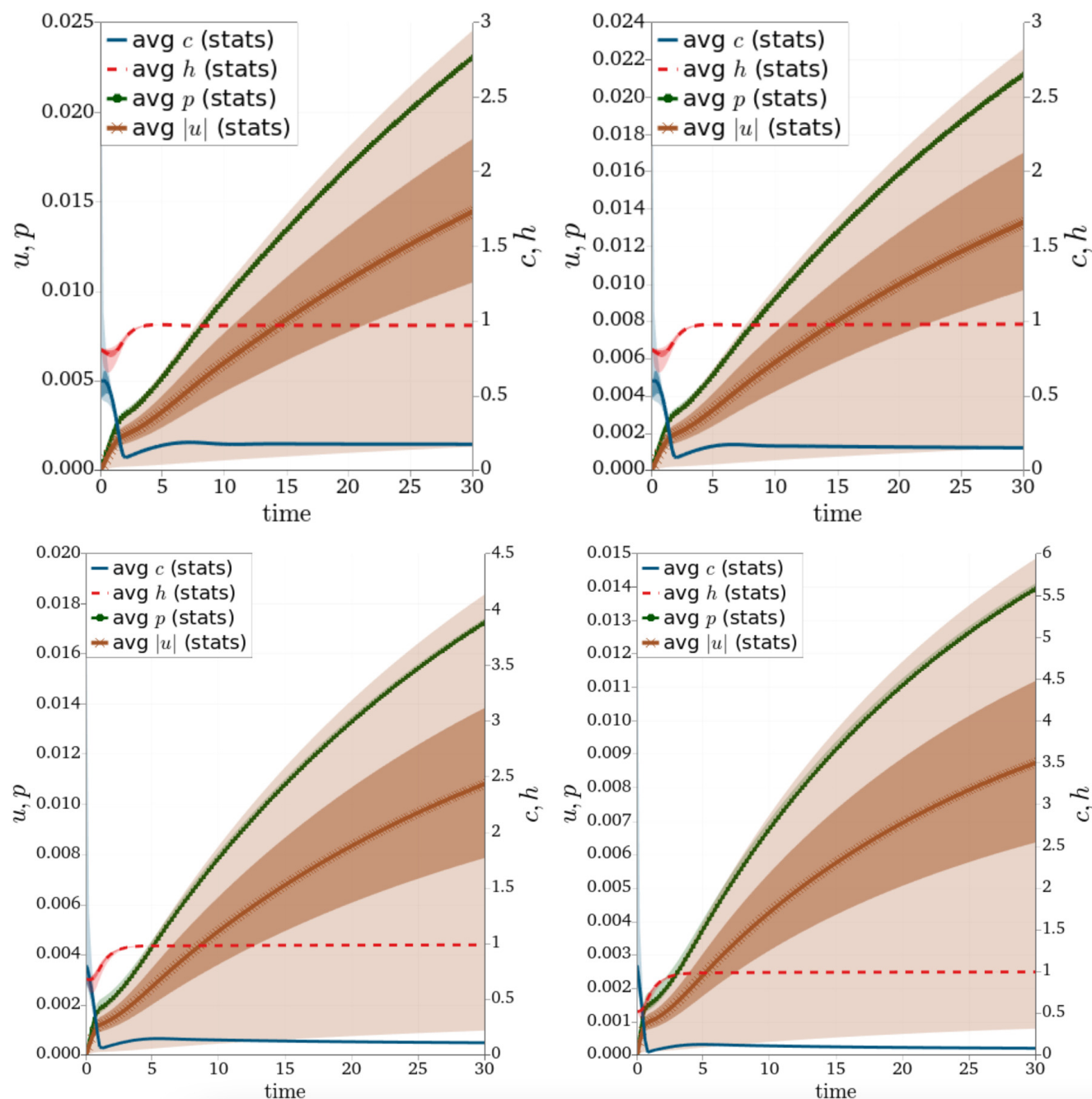


Figure 3.2. Plot over time of statistics (quartiles, ranges, and average) of field variables (the scales for calcium concentration and for the percentage of non-inactivated IPR are on the right axes, whereas the scales for the displacement magnitude and for the Herrmann pressure are on the left axes) at 80 points near the disk centre (square of side 0.25). Parameters are $\beta_1^{\text{in}} = 3.16$, $\mu = 0.288$ and $\lambda \in \{0.01, 0.1, 0.5, 1.3\}$, varied from top left to bottom right.

4 CONCLUSIONS

221 We propose a new mechanochemical model that reproduces important experimental findings on the
 222 apical constriction (AC) during the last stage of NTC. AC is controlled by the complex coupling of

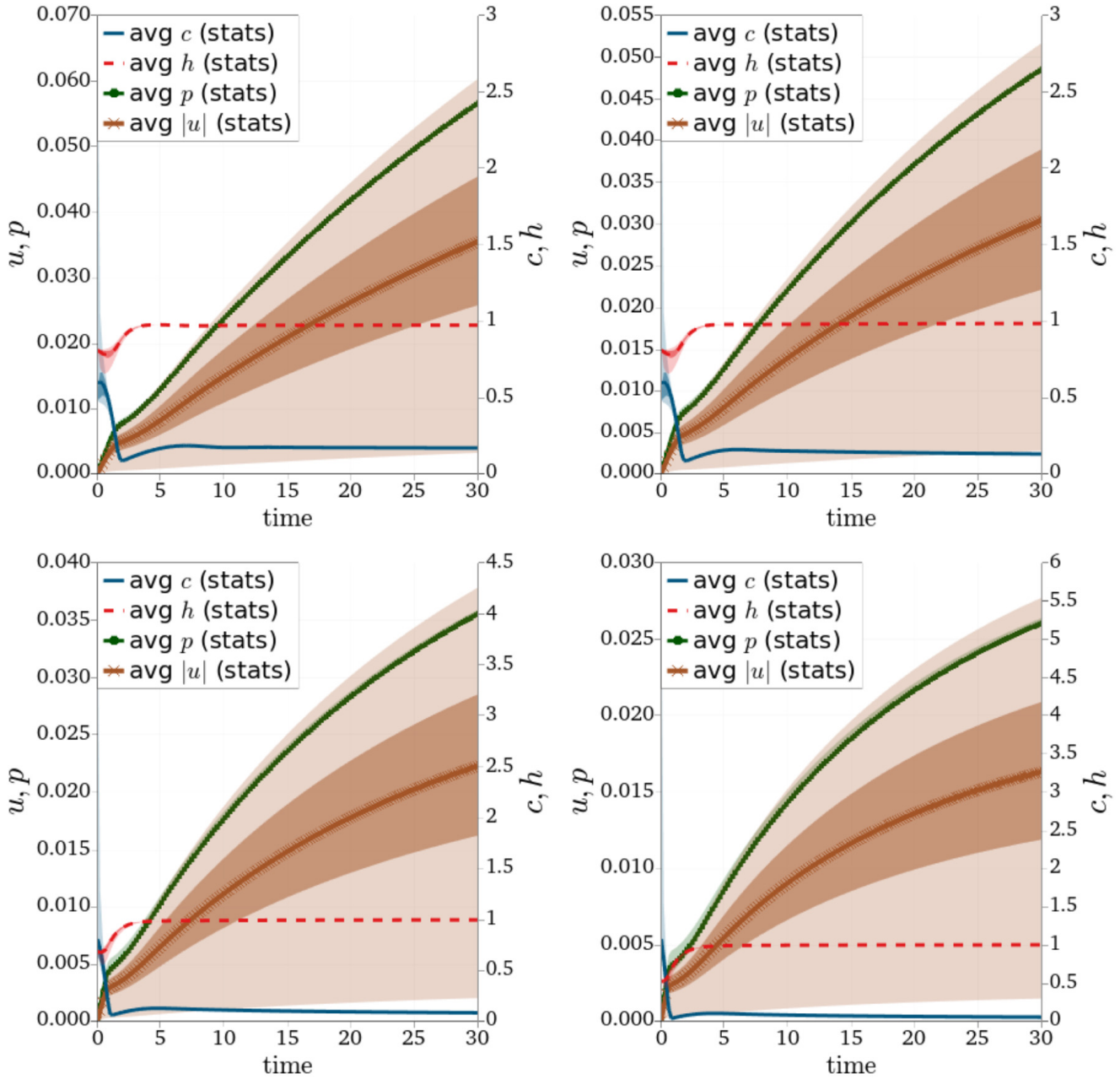


Figure 3.3. Plot of statistics (quartiles, ranges, and average) of the model variables over time, spatially averaged over 80 points near the disk centre (square of side 0.25). The scales for calcium concentration and for the percentage of open IPR are on the right axes, whereas the scales for the displacement magnitude and for the Herrmann pressure are on the left axes. Parameters are $\beta_1^{\text{in}} = 7.91$ ($T_0 = 250$ Pa), $\mu = 0.288$ and $\lambda \in \{0.01, 0.1, 0.5, 1.3\}$, varied from top left to bottom right panels.

223 calcium signalling to the mechanics of the embryonic epithelial tissue; disruption of calcium signals and
 224 consequently of AC leads to significant embryo malformations such as *Spina Bifida* and anencephaly.

225 The model builds on other recent mechanochemical models [20, 21]. The calcium-induced calcium
 226 release process allowing calcium to get released from the ER into the cytosol has been modulated with a
 227 random-in-space distribution of calcium sparks of which the amplitude and frequency increase with time

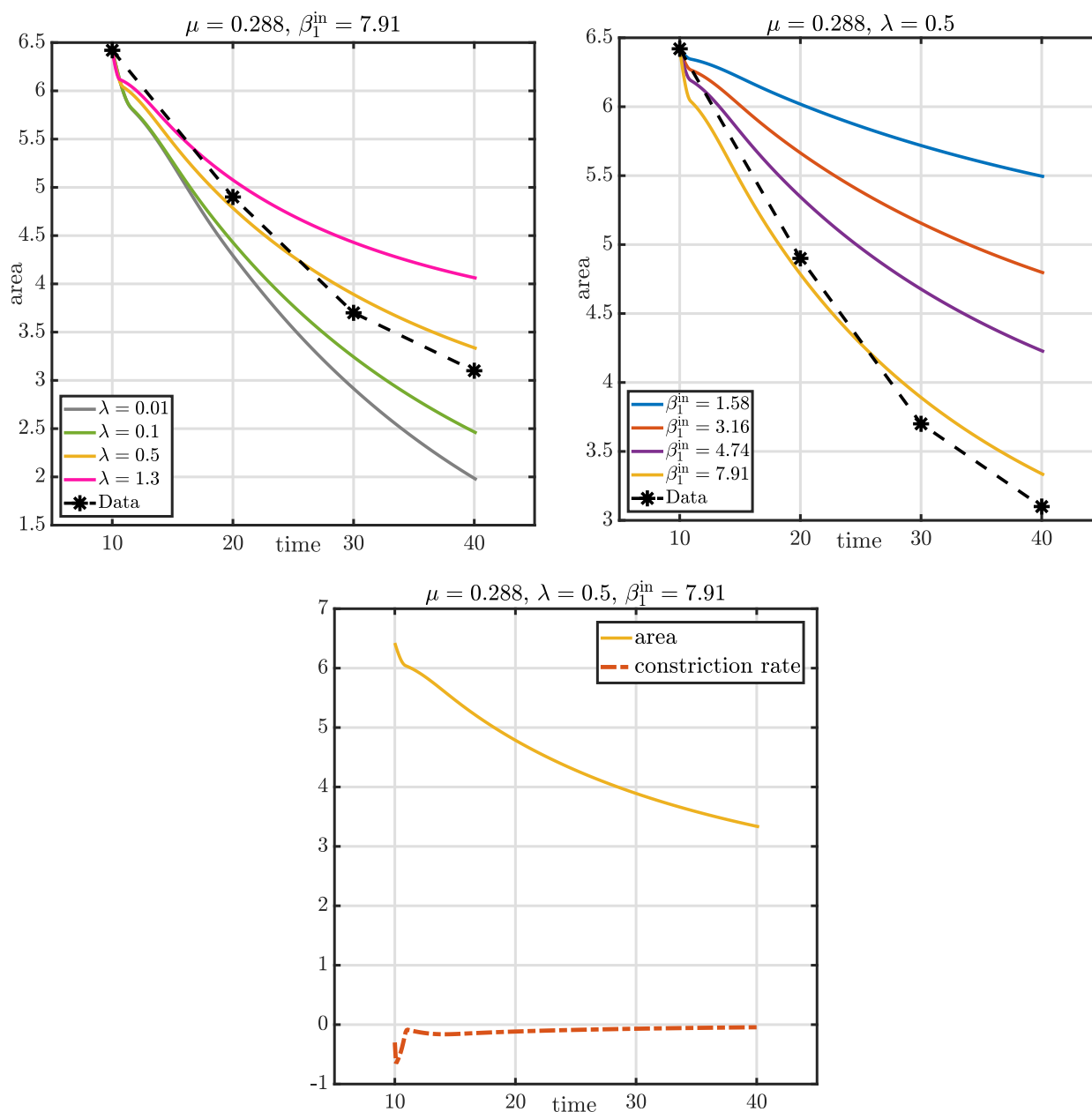


Figure 3.4. Area (in non-dimensional units) with respect to time for different parameter values, plotted against experimental data from [20]. The red, dash-dotted curve in the bottom plot depicts the approximately constant constriction rate, for the parameter set $\mu = 0.288$, $\lambda = 0.5$, $\beta_1^{\text{in}} = 7.91$.

228 which has been fitted to agree with experimental data presented in [20, 1]—see Figure 1.1 and Figure 3.1.
 229 The embryonic tissue is modelled as a linear viscoelastic material, including three types of stresses: viscous,
 230 elastic and an active contraction stress which increases with calcium concentration until it saturates.

231 We have simulated the model using a finite element method on a disc domain packing 256 epithelial cells
 232 – details about the numerical method can be found in [21]. We have studied the behaviour of the model as
 233 three parameters vary: μ , the level of IP_3 , λ , which measures the strength of the stretch-sensitive activation
 234 and β_1^{in} which represents the maximum contraction stress.

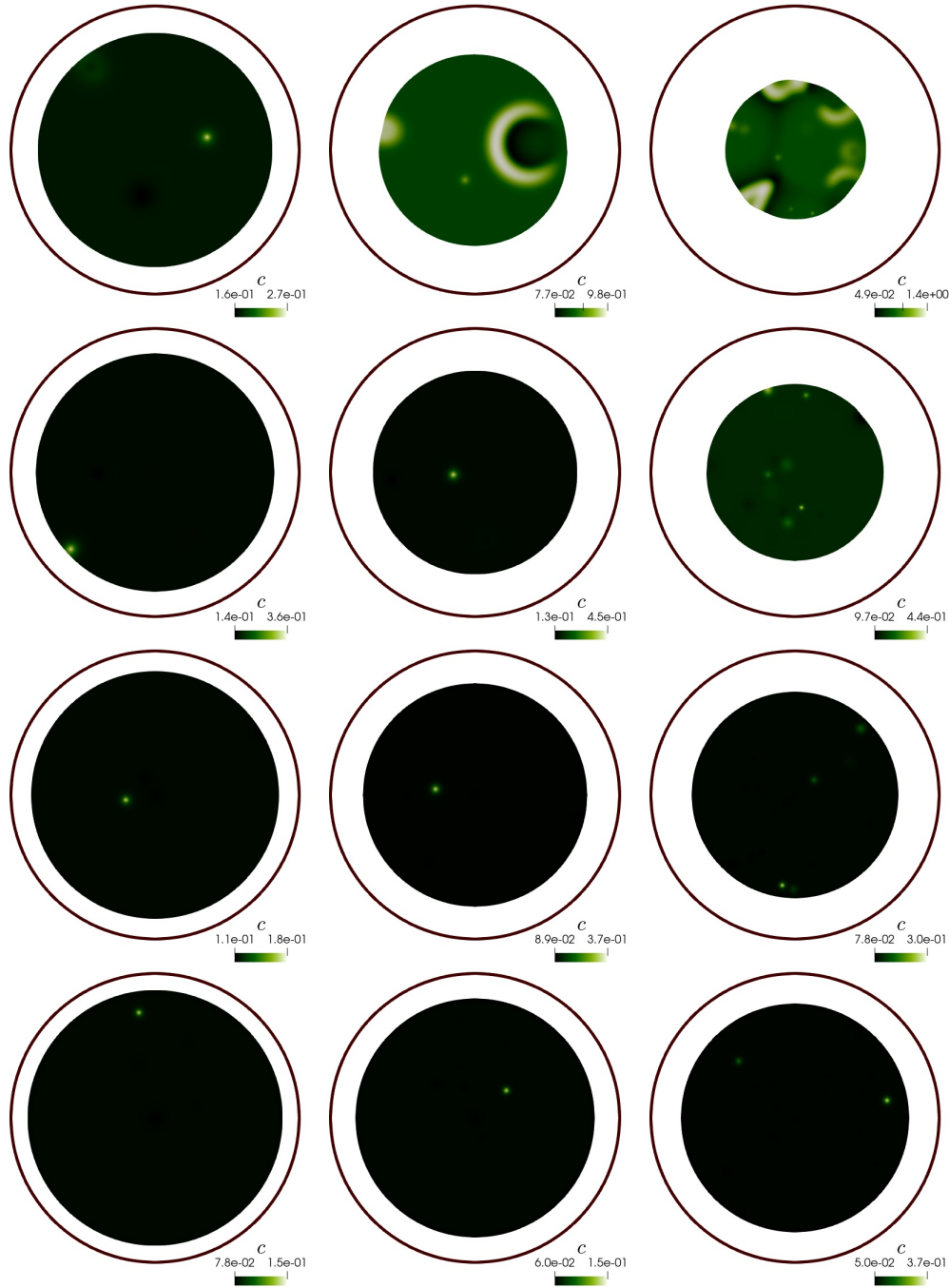


Figure 3.5. Snapshots of the contracting domain and the associated calcium distribution, at $t = 20, 30, 40$. Parameters are $\mu = 0.288$, and $\lambda = \{0.01, 0.1, 0.5, 1.3\}$ from top to bottom rows, respectively. Here we use $\beta_1^{\text{in}} = 7.91$.

235 The model shows that for any value of μ , λ and β_1^{in} the tissue area is decreasing monotonically over
 236 time, as observed in experiments [1, 2]. Furthermore, we have identified that for $\mu = 0.288$, $\lambda = 0.5$
 237 and $\beta_1^{\text{in}} = 7.91$, the monotonic area decrease fits to the experimental curve, generated in [1]. Also in
 238 Figure 3.4 (bottom plot) we have quantified and plotted the constriction rate (red, dash-dotted curve, which
 239 is approximately constant as observed in experiments [1].

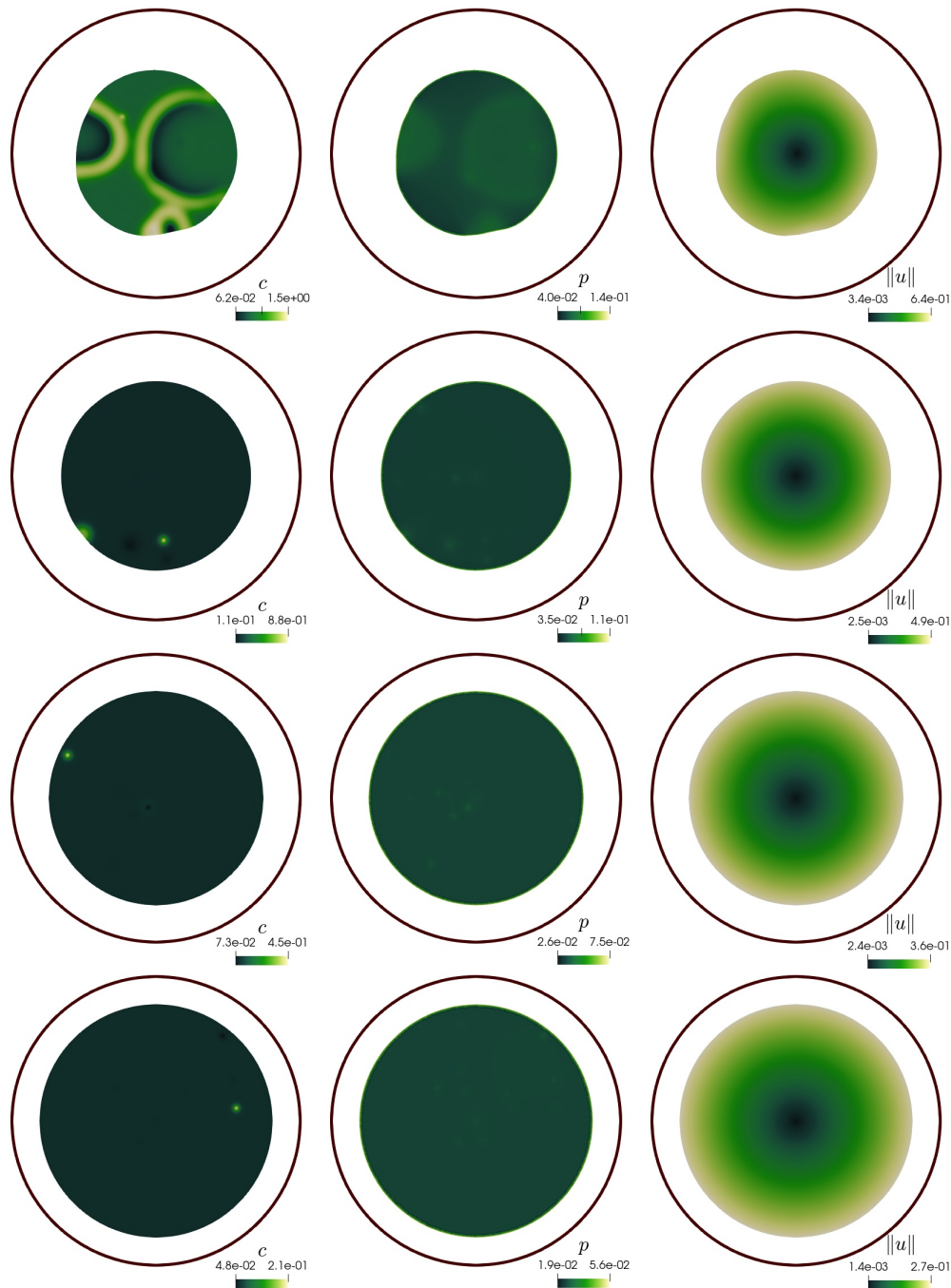


Figure 3.6. Snapshots of the contracting domain and the associated calcium distribution (left), Herrmann pressure (centre), and displacement (right), at time $t = 35$. Parameters are: $\mu = 0.288$, $\lambda = 0.01$ (top), $\lambda = 0.1$ (second row), $\lambda = 0.5$ (third row), $\lambda = 1.3$ (bottom), and using $\beta_1^{\text{in}} = 7.91$.

240 We also found that as λ increases the contraction effect decreases—see Figures 3.5 and 3.3. This result
 241 could be tested in future experiments.

242 Although real tissues usually show intermediate degrees of viscoelasticity [43, 44, 45, 46, 47] it is not
 243 uncommon that mechanical models of morphogenesis assume one of two extremes in material behaviour:
 244 either a purely elastic or a purely viscous fluid. For the specific case of embryonic tissues, in [48] authors
 245 conclude that most embryonic tissues should be considered viscoelastic in order to fully understand the

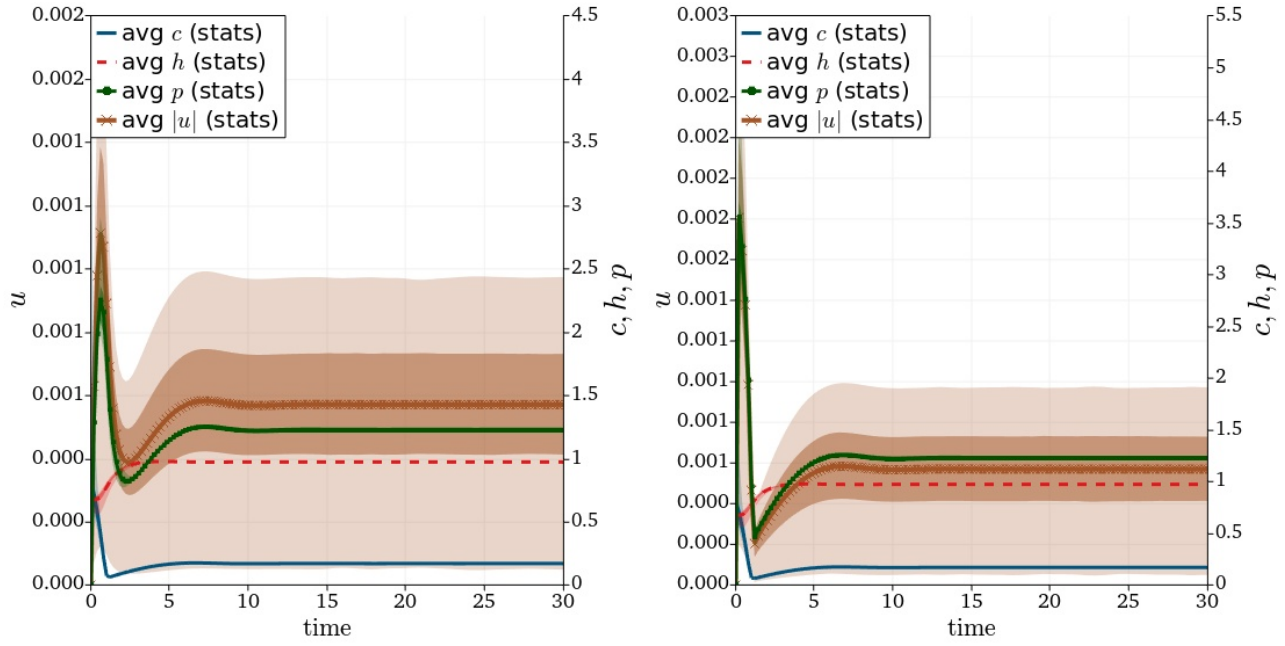


Figure 4.1. Testing behaviour in the nearly incompressible purely elastic and viscoelastic cases. Parameters are $\nu = 0.4999$, $\tilde{\alpha}_1 = 3790$, $\tilde{\alpha}_2 = 550$ (left); and $\nu = 0.4999$, $\tilde{\alpha}_1 = \tilde{\alpha}_2 = 0$ (right).

mechanisms behind deformation of a multicellular tissue in response to any force or stress. Along similar lines, in [43] it is noted that the stability and robustness of specific physical mechanisms of morphogenesis will likely have a strong dependence on the viscoelasticity of the tissue.

Here, for the stage of embryogenesis we consider (stage 16), we can assume small strains; hence we modelled the tissue as a linear Kelvin–Voigt viscoelastic material. However, we emphasize that the formulation we propose along with the finite element method we employ do accommodate for the pure elastic case and also for material constants close to the incompressibility limit. This is tested in the following simple example where we choose the parameters $\mu = 0.288$, $\lambda = 0.5$, $T_0 = 250$, and take a higher Poisson ratio ($\nu = 0.4999$) with or without shear-bulk viscosities. The results are visualised in Figure 4.1. They need to be compared with the base-line case shown in Figure 3.3 (bottom left panel). Both panels use $\nu = 0.4999$ (which corresponds to the slightly higher $\beta_1^{\text{in}} = 8.47$, since β_1 is proportional to the Poisson ratio). The left panel shows the behaviour when maintaining the base-line viscoelastic parameters. The displacement and pressure exhibit an initial peak and then return to a plateau phase. On the right panel we focus on the case with $\tilde{\alpha}_1 = \tilde{\alpha}_2 = 0$ (on both neuroepithelium and epidermis regions). Both calcium and the percentage of open IPR are quite similar to the base-line case. As in the left panel, both the Hermann pressure and the displacement exhibit an initial peak followed by an undershoot and then reach a plateau phase. However, the displacement magnitude is much lower than in the viscoelastic case (in the base-line case, both mechanical fields were increasing monotonically).

We also note that in order to properly capture other stages of NTC, we would require a large-strain viscoelasticity framework in combination with a remodelling approach. This constitutes a direction for future research.

CONFLICT OF INTEREST STATEMENT

The authors declare that the research was conducted in the absence of any commercial or financial relationships that could be construed as a potential conflict of interest.

AUTHOR CONTRIBUTIONS

All authors were involved in the conceptualisation and design of the mathematical model, the computational implementation, and in the analysis and interpretation of results. All authors have read, revised and approved the final manuscript.

ACKNOWLEDGEMENTS

We thank Prof. Lance Davidson, for fruitful discussions, in particular regarding choosing appropriate parameter values. We also thank Prof. Tim N. Phillips for useful discussions on the modelling of materials.

This work has been supported by the European Regional Development Fund and the Republic of Cyprus through the Research and Innovation Foundation (POST-DOC/0718/0087); by a Marie Skłodowska-Curie individual fellowship grant (101038073); by the Monash Mathematics Research Fund S05802-3951284; by the Australian Research Council through the Future Fellowship grant FT220100496 and Discovery Project grant DP22010316; and by the Ministry of Science and Higher Education of the Russian Federation within the framework of state support for the creation and development of World-Class Research Centers “Digital biodesign and personalised healthcare” No. 075-15-2022-304.

REFERENCES

- [1] Christodoulou N, Skourides PA. Cell-autonomous Ca^{2+} flashes elicit pulsed contractions of an apical actin network to drive apical constriction during neural tube closure. *Cell Reports* **13** (2015) 2189–2202.
- [2] Suzuki M, Sato M, Koyama H, Hara Y, Hayashi K, Yasue N, et al. Distinct intracellular Ca^{2+} dynamics regulate apical constriction and differentially contribute to neural tube closure. *Development* **144** (2017) 1307–1316.
- [3] Smedley MJ, Stanisstreet M. Calcium and neurulation in mammalian embryos: II. Effects of cytoskeletal inhibitors and calcium antagonists on the neural folds of rat embryos. *Journal of Embryology and Experimental Morphology* **93** (1986) 167–178.
- [4] Wallingford JB, Ewald AJ, Harland RM, Fraser SE. Calcium signaling during convergent extension in *Xenopus*. *Current Biology* **11** (2001) 652–661.
- [5] Herrgen L, Voss OP, Akerman CJ. Calcium-dependent neuroepithelial contractions expel damaged cells from the developing brain. *Developmental Cell* **31** (2014) 599–613.
- [6] Hunter GL, Crawford JM, Jenkins JZ, Kiehart DP. Ion channels contribute to the regulation of cell sheet forces during *Drosophila* dorsal closure. *Development* **141** (2014) 325–334.
- [7] Sanderson MJ, Charles A, Dirksen ER. Mechanical stimulation and intercellular communication increases intracellular Ca^{2+} in epithelial cells. *Cell Regulation* **1** (1990) 585–596.
- [8] Sanderson MJ, Chow I, Dirksen ER. Intercellular communication between ciliated cells in culture. *American Journal of Physiology-Cell Physiology* **254** (1988) C63–C74.
- [9] Sanderson MJ, Sleigh MA. Ciliary activity of cultured rabbit tracheal epithelium: beat pattern and metachrony. *Journal of Cell Science* **47** (1981) 331–347.

- [10] Charles AC, Dirksen ER, Merrill JE, Sanderson MJ. Mechanisms of intercellular calcium signaling in glial cells studied with dantrolene and thapsigargin. *Glia* **7** (1993) 134–145.
- [11] Charles AC, Merrill JE, Dirksen ER, Sandersont MJ. Intercellular signaling in glial cells: calcium waves and oscillations in response to mechanical stimulation and glutamate. *Neuron* **6** (1991) 983–992.
- [12] Charles AC, Naus C, Zhu D, Kidder GM, Dirksen ER, Sanderson MJ. Intercellular calcium signaling via gap junctions in glioma cells. *The Journal of Cell Biology* **118** (1992) 195–201.
- [13] Narciso CE, Contento NM, Storey TJ, Hoelzle DJ, Zartman JJ. Release of applied mechanical loading stimulates intercellular calcium waves in *Drosophila* wing discs. *Biophysical Journal* **113** (2017) 491–501.
- [14] Bereiter-Hahn J. Mechanics of crawling cells. *Medical Engineering & Physics* **27** (2005) 743–753.
- [15] Tsutsumi M, Inoue K, Denda S, Ikeyama K, Goto M, Denda M. Mechanical-stimulation-evoked calcium waves in proliferating and differentiated human keratinocytes. *Cell and Tissue Research* **338** (2009) 99–106.
- [16] Yang W, Chen JY, Zhou L. Effects of shear stress on intracellular calcium change and histamine release in rat basophilic leukemia (RBL-2H3) cells. *Journal of Environmental Pathology, Toxicology and Oncology* **28** (2009) 223–230.
- [17] Young S, Ennes H, McRoberts J, Chaban V, Dea S, Mayer E. Calcium waves in colonic myocytes produced by mechanical and receptor-mediated stimulation. *American Journal of Physiology-Gastrointestinal and Liver Physiology* **276** (1999) G1204–G1212.
- [18] Guiu-Souto J, Munuzuri AP. Influence of oscillatory centrifugal forces on the mechanism of Turing pattern formation. *Physical Review E* **91** (2015) 012917.
- [19] Lecuit T, Lenne PF. Cell surface mechanics and the control of cell shape, tissue patterns and morphogenesis. *Nature Reviews: Molecular Cell Biology* **8** (2007) 633–644.
- [20] Kaouri K, Maini PK, Skourides PA, Christodoulou N, Chapman SJ. A simple mechanochemical model for calcium signalling in embryonic epithelial cells. *Journal of Mathematical Biology* **78** (2019) 2059–2092.
- [21] Kaouri K, Méndez PE, Ruiz-Baier R. Mechanochemical models for calcium waves in embryonic epithelia. *Vietnam Journal of Mathematics* **50** (2022) in press.
- [22] Murray JD, Oster GF. Generation of biological pattern and form. *Mathematical Medicine and Biology: a Journal of the IMA* **1** (1984) 51–75.
- [23] Banerjee S, Marchetti MC. Instabilities and oscillations in isotropic active gels. *Soft Matter* **7** (2011) 463–473.
- [24] Atri A, Amundson J, Clapham D, Sneyd J. A single-pool model for intracellular calcium oscillations and waves in the *xenopus laevis* oocyte. *Biophysical Journal* **65** (1993) 1727–1739.
- [25] Nguyen TL, Polanco ER, Patananan AN, Zangle TA, Teitell MA. Cell viscoelasticity is linked to fluctuations in cell biomass distributions. *Scientific Reports* **10** (2020) 1–11.
- [26] Herrmann LR. Elasticity equations for incompressible and nearly incompressible materials by a variational theorem. *AIAA Journal* **3** (1965) 1896–1900.
- [27] Murray JD. *Mathematical biology II: spatial models and biomedical applications*, vol. 3 (Springer New York) (2001).
- [28] Murray JD. On the mechanochemical theory of biological pattern formation with application to vasculogenesis. *Comptes Rendus Biologies* **326** (2003) 239–252.
- [29] Neville A, Matthews P, Byrne H. Interactions between pattern formation and domain growth. *Bulletin of Mathematical Biology* **68** (2006) 1975–2003.

- [30] Ruiz-Baier R, Gizzi A, Rossi S, Cherubini C, Laadhari A, Filippi S, et al. Mathematical modelling of active contraction in isolated cardiomyocytes. *Mathematical Medicine and Biology: a Journal of the IMA* **31** (2014) 259–283.
- [31] D’Angelo A, Dierkes K, Carolis C, Salbreux G, Solon J. In vivo force application reveals a fast tissue softening and external friction increase during early embryogenesis. *Current Biology* **29** (2019) 1564–1571.e6.
- [32] Benko R, Brodland GW. Measurement of in vivo stress resultants in neurulation-stage amphibian embryos. *Annals of Biomedical Engineering* **35** (2007) 672–681.
- [33] Wiebe C, Brodland GW. Tensile properties of embryonic epithelia measured using a novel instrument. *Journal of biomechanics* **38** (2005) 2087–2094.
- [34] Moreo P, Gaffney EA, García-Aznar JM, Doblaré M. On the modelling of biological patterns with mechanochemical models: Insights from analysis and computation. *Bulletin of Mathematical Biology* **72** (2010) 400–431.
- [35] Zhou J, Kim HY, Davidson LA. Actomyosin stiffens the vertebrate embryo during crucial stages of elongation and neural tube closure. *Development* **136** (2009) 677–688.
- [36] Yamaguchi N, Zhang Z, Schneider T, Wang B, Panozzo D, Knaut H. Rear traction forces drive adherent tissue migration in vivo. *Nature Cell Biology* **24** (2022) 194–204.
- [37] Kraning-Rush CM, Califano JP, Reinhart-King CA. Cellular traction stresses increase with increasing metastatic potential. *PloS one* **7** (2012) e32572.
- [38] Oakes PW, Banerjee S, Marchetti MC, Gardel ML. Geometry regulates traction stresses in adherent cells. *Biophysical journal* **107** (2014) 825–833.
- [39] Zhou J, Pal S, Maiti S, Davidson LA. Force production and mechanical accommodation during convergent extension. *Development* **142** (2015) 692–701.
- [40] Langtangen HP, Logg A. *Solving PDEs in Python: The FEniCS Tutorial I*, vol. 1 (Oslo: Springer) (2017).
- [41] Amestoy PR, Duff IS, L’Excellent JY, Koster J. MUMPS: a general purpose distributed memory sparse solver. *International Workshop on Applied Parallel Computing* (Springer) (2000), 121–130.
- [42] Cioncolini A, Boffi D. The MINI mixed finite element for the Stokes problem: An experimental investigation. *Computers and Mathematics with Applications* **77** (2019) 2432–2446.
- [43] von Dassow M, Davidson LA. Physics and the canalization of morphogenesis: a grand challenge in organismal biology. *Physical Biology* **8** (2011) 045002.
- [44] Parvini CH, Cartagena-Rivera AX, Solares SD. Viscoelastic parameterization of human skin cells characterize material behavior at multiple timescales. *Communications Biology* **5** (2022).
- [45] Brückner BR, Janshoff A. Elastic properties of epithelial cells probed by atomic force microscopy. *Biochimica et Biophysica Acta (BBA) - Molecular Cell Research* **1853** (2015) 3075–3082.
- [46] Lange JR, Fabry B. Cell and tissue mechanics in cell migration. *Experimental Cell Research* **319** (2013) 2418–2423.
- [47] Karcher H, Lammerding J, Huang H, Lee RT, Kamm RD, Kaazempur-Mofrad MR. A three-dimensional viscoelastic model for cell deformation with experimental verification. *Biophysical Journal* **85** (2003) 3336–3349.
- [48] Davidson LA. Embryo mechanics. *Current Topics in Developmental Biology* (Elsevier) (2011), 215–241.